High-resolution resonant excitation of NV centers in 6*H*-SiC: A matrix for quantum technology applications

Kh. Khazen,[1,2] H. J. von Bardeleben,[1] S. A. Zargaleh,[3] J. L. Cantin,[1] Mu Zhao,[3]
Weibo Gao,[3] T. Biktagirov,[4] and U. Gerstmann[4]

[1]*Sorbonne Université, Campus Pierre et Marie Curie, Institut des Nanosciences de Paris, 4, place Jussieu, 75005 Paris, France*
[2]*Quantum Matter and Technology Laboratory, Department of Converging Technologies, PIAIS-Khatam University, Tehran, Iran*
[3]*The Photonics Institute and Centre for Disruptive Photonic Technologies, Nanyang Technological University, Singapore 637371, Singapore*
[4]*Department of Physik, University of Paderborn, Warburger Strasse 100, 33098 Paderborn, Germany*

(Received 31 August 2019; published 11 November 2019)

Atomlike defect levels in silicon carbide (SiC) polytypes have been proposed and proven to be an excellent platform for various quantum technology applications. Single-photon emitters, coherent control at room temperature, and temperature and magnetic field sensing at the nanoscale have already been demonstrated for the case of vacancy and divacancy defects in SiC and more recently proposed for negatively charged NV centers. NV centers, which allow a better control of their generation, offer in addition a further shift of the spectral range in the near infrared, i.e., in the *O*- and *S*-band telecom range. We demonstrate here that the association of high resolution optical spectroscopy and electron paramagnetic resonance spectroscopy combined with *first-principles* calculations allow the identification of the microscopic structure of the six distinct NV centers in 6*H*-SiC and the assignment of their associated zero-phonon photoluminescence lines. Time resolved photo-EPR measurements at $T = 4$ K show that NV centers in 6*H*-SiC present spin lattice relaxation times of several seconds. These excellent qubit properties should enable their application and implementation in quantum information devices.

DOI: 10.1103/PhysRevB.100.205202

I. INTRODUCTION

The implementation of various quantum technology proof-of-concepts based on atomlike defect centers in silicon carbide have attracted much attention in the past few years. Whereas the NV^- center in diamond seems to be the favorite choice for such applications [1], the material properties of diamond are not optimal for large-scale integration, and recently silicon carbide (SiC) has been proposed as an interesting alternative, due to its mature microelectronic properties [2–8]. Since then, an intense research effort focusing on three vacancy related intrinsic defects in SiC has confirmed these predictions: they are the negatively charged silicon monovacancy (V_{Si}), the neutral silicon-carbon divacancies ($V_{Si}V_C$), and the negatively charged NV centers (N_CV_{Si}) [9–34]. Their basic properties, such as the polytype dependence of their optical and spin properties [12], their spin coherence times [16,27], and the influence of neighboring nuclear spins [14,17,23,25], have been the object of the earlier studies. Room temperature coherent control has been demonstrated by various authors [9,10,18,21]. Room temperature quantum entanglement has been achieved for the PL6 center in 4*H*-SiC [22]. Magnetic field sensing and thermometry at a nanoscale has been demonstrated for the V_{Si} center [15,31]. Enhancing the optical properties by embedding these defects in photonic cavities has been shown [13,24] as well as the tuning of their spin properties by electric fields [19,30]. Single photon emission has been shown for defects in different SiC polytypes [26,33]. These major achievements make intrinsic defects in SiC interesting competitors to the NV^- center in diamond [35].

We have shown recently [36–41] that also the direct analog of the NV^- center in diamond, the NV^- centers in SiC, can be generated in all three main polytypes 3*C*, 4*H*, 6*H* of SiC. In SiC the NV center is a silicon vacancy nitrogen nearest neighbor pair with structural similarity to the case of diamond. The identification of the NV^- centers in SiC was based on EPR studies, combined with *ab initio* calculations of their spin Hamiltonian parameters [36,37]. In the hexagonal polytypes, due to the lower symmetry of the crystal, different NV center configurations coexist: four (4*H*) and six (6*H*) distinct NV, respectively. Like the original NV center in diamond, all the NV centers in SiC have in their 1– charge state a similar electronic structure with a $^3A_2$ ground state and ^3E excited state, both with spin $S = 1$. Most important, they also present an intermediate singlet state, which allows an optical induced spin polarization of the ground state. However, their optical properties are shifted from the visible in diamond into the near infrared (NIR), making them more suitable for transmission in fibers, a further advantage for applications. In contrast to intrinsic defects like divacancies, both well localized single NV centers and spatially controlled arrays of NV centers can be generated in SiC by nitrogen implantation [34]. Moreover, the possibility of electrical excitation of NV centers due to the semiconducting properties of SiC is a further advantage of SiC over diamond.

Ab initio calculations of the electronic properties have shown that NV centers in SiC are stable in several charge

states. Their charge state is thus related to the Fermi-level position, a parameter, which has to be controlled just as for the NV center in diamond. In *n*-type material with a Fermi level pinned on the nitrogen shallow donor, the NV centers in 6*H*-SiC will be in the *wrong* 2– charge state, but partial electrical compensation or applying reverse bias in space charge regions will favor the interesting 1– charge state. The case of NV centers in 3*C* polytype is more favorable, as due to its smaller band gap the 2– charge state is not stable and the desired 1– charge state of the NV center is already obtained in *n*-type conducting material [39].

Most of the previous studies on color centers in SiC were based on low temperature optical spectroscopy where narrow ZPL were resolved and the spin coherence times of milliseconds were observed [16]. Extension to room temperature spectroscopy has nevertheless been obtained for two centers, called PL5 and PL6, which have similar electronic properties to the divacancy centers. However, the microscopic structure of the PL5, PL6 centers is still unknown. It is clear, however, that they are not simple divacancies in the 4*H* polytype as often tacitly assumed [22]. They have been detected as native defects in semi-insulating bulk 4*H*-SiC but as their microscopic structure is unknown; they cannot be purposely generated up to now and they have not been related to irradiation treatments. There has been the proposition that they might be related to 6*H* polytype inclusions in 4*H* bulk samples. Thus, NV centers in the 6*H* polytype might present certain advantages. The demonstration of room-temperature entanglement of the PL6 center in 4*H*-SiC [22] is an additional motivation for their study.

In this work, using EPR-tagged high resolution excitation spectroscopy (EPR-RES), we demonstrate the possibility to address selectively the different NV^- centers in 6*H*-SiC using the very narrow intracenter transitions $^3A \rightarrow {}^3E$, which can be monitored via EPR due to the related optically induced ground state spin polarization. DFT calculation of the zero-field splitting parameters (*D*, *E*) allow us to attribute the paramagnetic NV centers to specific defect configurations and EPR-RES spectroscopy to associate with the ZPL lines. The attribution is further confirmed by the direct calculation of the vertical excitation energies. These measurements have to be done at low temperature in order to observe the narrow zero phonon lines with high intensity. However, coherent control of NV^- centers in 4*H*-SiC have also been demonstrated at room temperature [42].

II. COMPUTATIONAL METHODS

First-principles calculations were performed in the framework of density functional theory (DFT) using the QUANTUM ESPRESSO package [43,44]. Exchange-correlation effects of the electronic system have been described with the semilocal Perdew-Burke-Ernzerhof (PBE) functional [45], projector-augmented wave (PAW) pseudopotentials [46]. The axial and basal configuration of the negatively charged NV pairs have been modeled with periodic boundary conditions using *symmetric* 324- and 648-atom supercells of *hexagonal shape*. Based on fully relaxed ground-state geometries (forces below 0.01 eV/A) we calculated the full magnetic signature of the spin-triplet state of the $N_C V_{Si}{}^-$ pairs. To obtain accurate

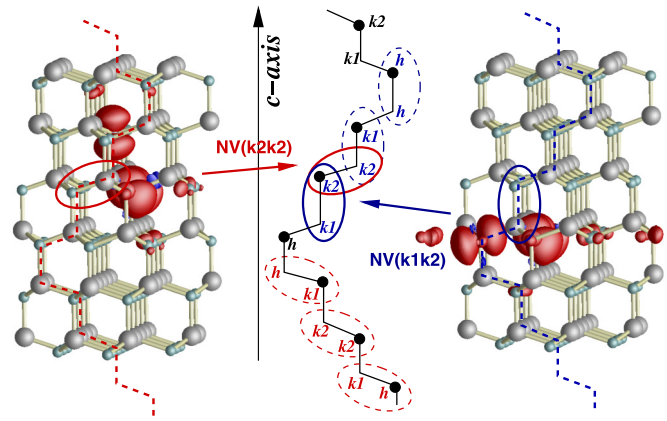

FIG. 1. Crystal structure of 6*H*-SiC showing the three nonequivalent Si and C (black circles) lattice sites, hexagonal (*h*) and quasicubic (*k*1 and *k*2), whereby *k*1 is always neighboring one *k*2 and three *h* sites (*k*2 has quasicubic neighbors exclusively). Thus we obtain the following NV center configurations: *basal*: *hk*1, *k*2*k*2, *k*1*h* and *axial*: *hh*, *k*2*k*1, *k*1*k*2 (for further details see the text). As an example we show also the magnetization density of the *basal* (*k*2*k*2, left) and the *axial* (*k*1*k*2, right) NV pair providing C_{1h} and C_{3v} symmetry, respectively.

estimates for the *g* tensors, hyperfine (HF) splittings, as well as the *D* and *E* value of the zero-field splitting (ZFS), we used scalar relativistic, norm-conserving gauge-including (GI) PAW pseudopotentials. In the calculations of the ZFS parameters the effects of the spin-orbit interaction has also been considered providing rather small contributions below 60 MHz (<4%) to the dominating spin-spin part. The spin-spin part is due to dipole-dipole interaction of the two-particle density [47] and tends to be overestimated by the so-called *spin contamination* [48], a spurious kind of antiferromagnetic spin polarization. In order to provide reasonable estimates for *D*, *E* allowing a better comparison with the experimental data, we correct the D_{SS} tensors for this effect [49]. For the calculation of the vertical excitation energies (ZPL absorption) we apply the same procedure used in [41] for the NV centers in 4*H*-SiC. Convergence of the EPR parameters as well as of the vertical excitation energies are obtained for $3 \times 3 \times 3$ *k*-point sampling and a plane-wave basis set with 680 eV energy cutoff.

In Fig. 1 we show the 6*H* polytype crystal structure with the indication of the three distinct lattice sites labeled *h*, *k*1, *k*2 corresponding to the hexagonal and two quasicubic sites, respectively. Note that *k*1 is always neighboring an *h* site, independent of the atomic occupation of the respective sublattice (see Fig. 1). The labeling is important as it allows us to distinguish and to classify the six different NV center configurations, which can be obtained by N occupying a carbon lattice site and being associated with a nearest neighbor silicon vacancy. The notation *k*1*k*2, e.g., corresponds to N on a *k*1 site (carbon sublattice) and the Si vacancy on the neighboring *k*2 site (Si sublattice). Thus, the three axial and three basal NV centers correspond to the following combinations: *axial* *hh*, *k*2*k*1, *k*1*k*2 and *basal* *hk*1, *k*2*k*2, *k*1*h*. It should be noted, however, that in some previous publications [39,51] these labels have been used in a slightly different way (*k*1 and *k*2

TABLE I. Photoluminescence ZPL lines of the six VV° and six NV⁻ centers in 6*H*-SiC. As in the case of VV° (QL5/QL6), the ZPL lines of two of the NV⁻ centers (NV2a/NV2b) are degenerate [see Fig. 1(b)]; thus, only five ZPL are resolved. For further assignment of the NV emission, see also Table III.

Label V_{Si}-V_C	VV^0 ZPL emission (nm) Expt. [12]	VV^0 ZPL emission (nm) Theory [51]	Symmetry/ orientation	NV ZPL emission (nm) Expt. (thiswork)	Label N_C-V_{Si}
QL1	1139	1320	axial	1227.3	NV4
QL2	1135	1329	axial	1182.6	NV2a
QL6	1093	1308	axial	1155	NV1
QL3	1124	1313	basal	1242	NV5
QL4	1108	1290	basal	1204	NV3
QL5	1093	1275	basal	1183	NV2b

interchanged for the C sublattice exclusively). For the sake of simplicity, if citing the respective labels are translated into the notation used throughout the present paper [50].

III. EXPERIMENTAL DETAILS

6*H*-SiC nitrogen doped bulk samples have been commercially purchased from different suppliers. Typical thickness is 400 μm and the typical sample size 5 $\times$ 5 mm^2. NV centers are not native defects in such material and we introduced them in the classical procedure of high energy particle irradiation followed by a thermal annealing step. We irradiated the samples at room temperature with high energy (2 to 12 MeV) electrons or protons, which due to elastic collisions and electronic excitation will form silicon and carbon vacancies and interstitials. Typical fluences are 10^{15}to10^{17} particles /cm^2. In a second step, the samples were annealed at 900°C to initiate the diffusion of the Si vacancies, which are mobile in this temperature range, and will form complexes with the doping related N centers, which are stable at this temperature. The NV center concentration is thus controlled by the N doping level. In parallel to the NV centers, divacancy centers will also be formed due to the presence of carbon vacancies equally generated by the irradiation process.

The EPR measurements have been performed with a Bruker *X*-band spectrometer under standard conditions with 100 kHz field modulation. Whereas the NV centers can be observed in the whole temperature range from $T = 300$ to 4 K the optical excitation measurements have all been performed at $T = 4$ K. To selectively excite the NV centers, we have used a tunable infrared single mode laser with a tuning range from 1170 to 1260 nm, a wavelength precision of 0.05 nm, and a maximum power of 30 mW. The linewidth was computer controlled and had been calibrated with a wavemeter.

The photoluminescence measurements were performed on the same samples at $T = 10$ K using nonresonant excitation of a 1000 nm diode laser beam, which was focused on the sample through a 0.5 Na microscope objective. The emitted photons were then dispersed by a 0.5 m focal lens monochromator and detected with an InGaAs diode.

IV. EXPERIMENTAL RESULTS

Figure 2 presents the wide range photoluminescence PL spectrum from 1050 to 1350 nm of an irradiated and annealed bulk sample. In the shorter wavelength range (1050–1150 nm), the previously reported zero phonon lines (ZPL) Q1-Q5 [12] are observed (Table I). They had not been identified initially as the PL and ODMR data alone allowing us only to determine the symmetry of the associated defects (axial/basal) but not their microscopic structure. Later, they have been tentatively associated with the negatively charged divacancies ($V_{Si}V_C$) based on the comparison with EPR results, which give additional information on the microscopic structure of the defects, when combined with theory to interpret the spin Hamiltonian parameters. The association of these ZPL with the divacancy centers seems now to be fairly well established [51]. In the higher wavelength range, five new ZPL labeled NV1–NV5 are observed, which, as we will show, are associated with the $N_CV_{Si}^-$ centers. Higher resolution measurements show the NV2 ZPL to be a doublet (NV2a,b). The energy of these ZPL is in good agreement with the range

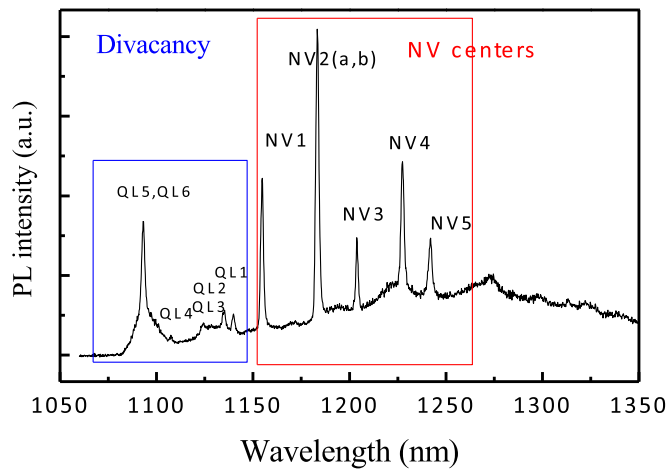

FIG. 2. High-resolution photoluminescence spectrum of 6*H*-SiC displaying under nonresonant excitation the ZPL of the VV° and NV⁻ centers; $T = 10$ K, optical excitation at 1000 nm. On the left (smaller wavelength), the PL corresponding to the divacancy centers are shown in the small (blue) rectangular frame; on the right (for larger wavelength) the NV center PL peaks are framed by the larger (red) rectangle. We observe five ZPL as two ZPL (NV2a/NV2b) are nearly degenerate at 1183 nm and not resolved in this PL spectrum. This is also the case for the VV° ZPL where two ZPL QL5/QL6 are nearly degenerate.

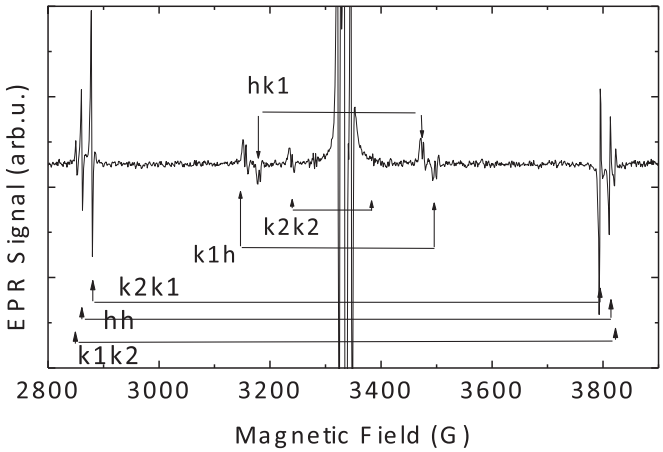

FIG. 3. *X*-band EPR spectrum for $B//c$ and $T = 4$ K displaying the six doublet spectra of the three axial and three basal spin $S = 1$ NV^- centers (see also Fig. 1). Basal spectra can be easily identified: due to their off-axis orientation, their resonance fields are very different for the orientation of $B//c$.

0.96 to 1.00 eV, predicted by previous *ab initio* calculations [36–41].

The same samples studied by photoluminescence have been investigated by EPR spectroscopy. In Fig. 3 we show a large-scale EPR spectrum for the orientation of the applied magnetic field $B//c$ which is taken under optical excitation in order to increase the EPR signal intensity. For an excitation with 980 nm, it displays predominantly the six NV^- centers. Due to their different spin Hamiltonian parameters, they give rise to six distinct doublet spectra, corresponding to the $ms = 0 \rightarrow +1$ and $ms = 0 \rightarrow -1$ magnetic dipole transitions of each spin $S = 1$ center. The axial and basal NV centers can be directly distinguished for this orientation of the applied magnetic field as they provide clearly different splittings (Fig. 3). The use of the nonresonant 980 nm optical excitation allows us to display all six centers simultaneously. The optical excitation increases the EPR signal intensity from its thermal equilibrium value due to the optically induced ground state spin polarization induced by the recombination process from the excited ^3E state. Therefore, the phases of the low-field and high-field EPR transitions are inverted, and we observe the low-field lines in absorption and the high-field lines in emission. To extract the corresponding spin Hamiltonian parameters, given in Table II, we measured for each center the angular variation of the resonance fields as shown in Fig. 4(a). As in the case of the NV centers in 3*C* and 4*H*-SiC, the superhyperfine (SHF) interaction with the ^{14}N atom (nuclear spin $I = 1$) of the NV center is directly resolved in the EPR spectra for both the axial and basal centers [Fig. 4(b)]. The resulting triplet structure [Figs. 4(c) and 4(d)] presents a fingerprint of the NV centers and allows an easy distinction from the divacancy centers, which have almost the same spin distribution [36] and thus similar spin Hamiltonian parameters, but of course no ^{14}N SHF, thus resulting in a single central line EPR spectrum.

The experimental ZFS parameters of the NV^- centers, obtained by an angular variation of the EPR spectra for a rotation in the (11-20) and (1100) planes, are presented in Table II. They are compared to the predicted values from first-principle calculations (see Sec. II).The assignment of the six NV^- centers to the specific microscopic configuration is based on the comparison with the calculated and measured zero-field splitting parameters (*D*,*E*) and the SHF interaction with the ^{14}N nuclei. We see that the calculated ZFS parameters *D*, even though being systematically 3%–5% lower than the values measured at $T = 4$ K, reproduce well the experimental values and thus allow their assignment. This assignment will be further confirmed, as explained below, by the agreement between the calculated and experimental ZPL energies.

The electronic spins of the NV centers [as is the case of the divacancy (VV) centers] are mainly localized on the three nearest neighbor carbon atoms of the Si vacancy [see also Fig. 1(a)]; they give rise to the central HF interaction. The natural abundance of the ^{13}C isotope is small (1.1%) but the central hyperfine interaction could be resolved for the strongest NV^- center ($k2k1$) [Fig. 4(b)]. The corresponding splitting of 51 MHz for $B//c$ is in agreement with the theoretical predictions (see Table II and Ref. [37]). Superhyperfine (SHF) interactions of about 10 MHz with ^{29}Si nuclei are also visible [see, e.g., blue spectrum in Fig. 4(b)]. Like the *g* tensor these Si-related hyperfine interactions are basically identical for all six NV^- centers (see also Ref. [37]) and will not be discussed in more detail here.

Previously, it has been shown that nuclear spins can play a major role as safe storage units of quantum information (quantum memories), whose interaction with the electronic spins (qubits) form a complete package (spinbus) for quantum information processing [18]. The superhyperfine interactions

TABLE II. Spin Hamiltonian parameters (experimental and DFT calculated) of the six NV^- centers in 6*H*-SiC: zero-field splitting parameters *D*,*E*, hyperfine splitting *A* for the (SHF) interaction with ^{14}N, and central hyperfine interaction parameter $A_{//c}(^{13}C)$. All values are in MHz; experimental data given for $T = 4$ K.

NV center	ZFS_{expt} *D*,*E*	ZFS_{DFT} *D*,*E*	HF_{expt} $\lvert A\rvert(^{14}N)_{expt}$	HF_{DFT} $A(^{14}N)_{DFT}$	HF_{expt} $A_{//c}(^{13}C)_{expt}$	HF_{DFT} $A_{//c}(^{13}C)_{DFT}$
hh	1340	1298	1.32	−1.08	–	65.3 (3×)
k_2k_1	1289	1266	1.21	−1.12	51	58.1 (3×)
k_1k_2	1367	1324	1.02	−1.02	–	66.8 (3×)
k_2k_2	1321/138	1259/144	1.00	−0.86	–	116.9/74.1 (2×)
k_1h	1346/∼20	1280/10	1.00	−0.96	–	130.0/69.1 (2×)
hk_1	1247/∼20	1187/21	0.67	−0.59	–	128.5/65.5 (2×)

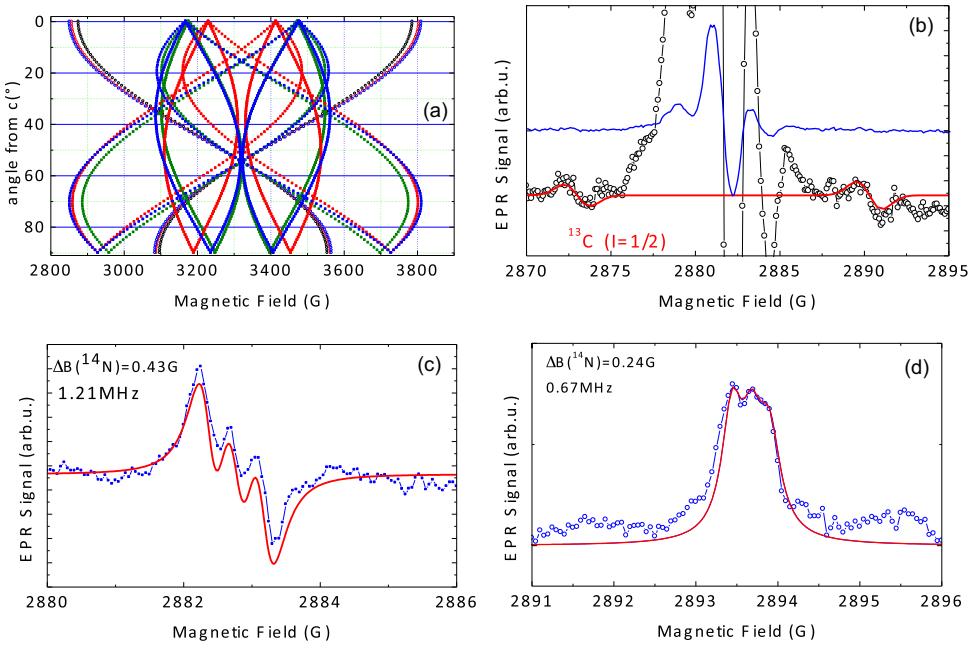

FIG. 4. EPR spectra of the NV$^-$ centers at $T = 4$ K under nonresonant excitation displaying the six NV$^-$ centers. (a) Angular variation of the six NV centers for a rotation of the magnetic field from $B//c$ to $B//[11\text{-}20]$, allowing the determination of the spin Hamiltonian parameters compiled in Table II. (b) For the highest-intensity axial NV center ($k2k1$) the central hyperfine interaction with one ^{13}C nucleus (one of the three C neighbors) is resolved (blue); (red line): spectrum multiplied by 200. (c) Higher resolution EPR spectrum of the axial NV center ($k1k2$) displaying directly the SHF interaction with nuclear spin $I = 1$ of the ^{14}N neighbor. (d) EPR spectrum of the $hk1$ basal NV center showing a strongly reduced SHF with ^{14}N as compared to the other NV centers.

have a very particular configuration for the case NV centers in 6*H*-SiC (e.g., compared to diamond), as the higher spatial distance between the interacting sites prevents strong interactions, which would disturb the information stored on the nuclear spins. The values, both experimental and theoretical, of the ^{14}N hyperfine interaction parameters and the CHF interactions with the three C neighbors are shown in Table II.

Time resolved EPR measurements under optical excitation allow us also to investigate the spin-lattice relaxation times. We have measured the decline of the ground-state spin polarization after cutoff of the optical excitation for the six NV$^-$ centers at $T = 4$ K. The measured transient behavior of the polarization can be simulated with a single exponential decay function characterized by a time constant t_1. The results, shown in Figs. 5(a) and 5(b), indicate exceptionally long spin lattice times T_1 of their ground state of the order of several seconds. These measurements were done on an ensemble of NV$^-$ centers, thus the T_1 times of individual NV$^-$ centers can be expected to be even longer. The spin relaxation times, which are longer than those of the divacancy centers, make NV$^-$ centers extremely attractive candidates for quantum technology (QT) applications. More information on the spin coherence times require time resolved ODMR measurements with pulsed (optical, microwave) sequences and single defect spectroscopy.

A. Qubit addressing

The assignment of each ZPL line to a specific NV$^-$ center is crucial to leverage the selectivity of optical addressing of a particular defect center as a qubit. This is, however, not achievable using only photoluminescence spectroscopy. Pre-

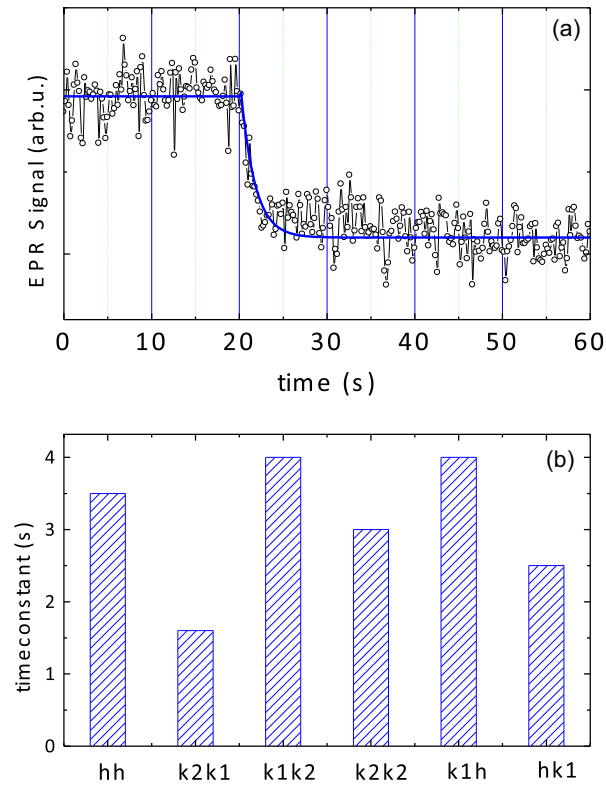

FIG. 5. (a), left: Transient behavior of the EPR signal of the axial $k2k1$ NV$^-$ center after switch-off of the optical excitation at $t = 20\,s$; $T = 4$ K, circles experiment, blue line fit with a single exponential decay. (b), right: Time constants of the relaxation time of the optically induced ground state spin polarization of the six NV$^-$ centers; $T = 4$ K.

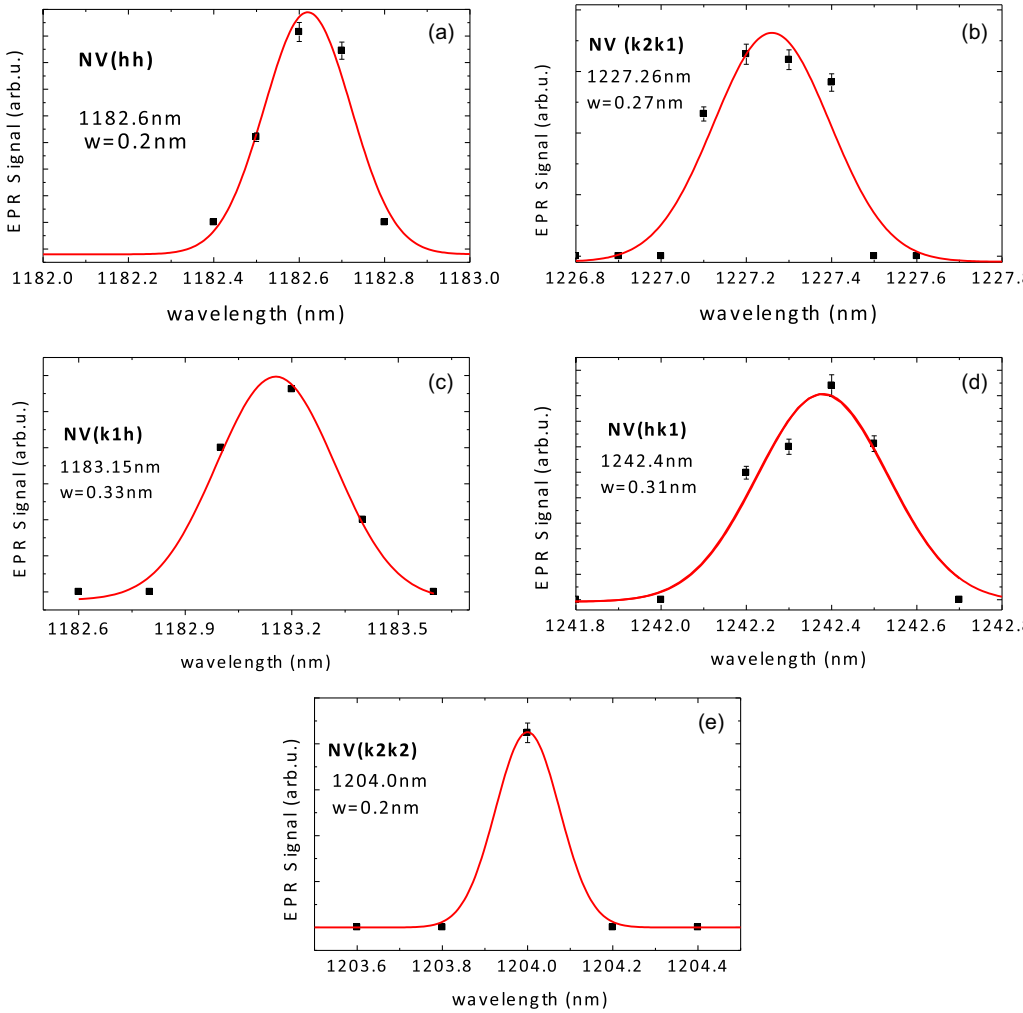

FIG. 6. (a)–(e) Resonant excitation EPR spectra measured (at $T = 4$ K) individually for each NV^- center on its low field EPR line. These spectra correspond to the ZPL absorption lines of the NV centers; the ZPL expected at 1155 nm is out of range of the tunable NIR laser but can be attributed from the knowledge of the other five ZPL lines.

viously, the assignment based only on theoretical predictions of the ZPL emission energies has shown its limit, due to the challenges in an accurate description of the Jahn-Teller distorted excited state [52] and, by this, still too high *relative* uncertainties in earlier calculations [36–39]. Moreover, as the range of the ZPL energies of the different NV defects is small as compared to the LO phonon energies, resonant PL excitation measurements with a detection via the phonon side bands will result in the mixing of phonon sidebands, destroying reliable readout processes. However, resonant optical excitation of the NV centers in their zero-phonon line and detection via EPR enables selective addressing of the specific center and allows us to overcome this problem. In parallel, it facilitates a theoretical treatment [41] as the excitation energies are not affected by Franck-Condon shifts.

The resonant excitation EPR measurements were performed on the low-field line of each NV^- center (Fig. 2). We measured the EPR signal intensity of each center while scanning the excitation wavelength over the different ZPL lines. We had already reported in our previous studies of NV centers in 4*H*-SiC [41] that the optical excitation, which monitors the absorption ZPL line of the $^3A \rightarrow {}^3E$ intracenter transition, is resonant with the ZPL emission line. We observe the same result for the NV^- centers in the 6*H* polytype. This is different from the case of the NV^- center in diamond for which a Stokes shift of 200 meV has been observed [53]. The intensity of the EPR signal is measured as a function of the laser wavelength, which is scanned in steps of 0.05 nm. The results are shown in Fig. 6 and Table III.

The wavelength scanning (cf. Fig. 6) demonstrates (i) the absorption ZPL are resonant with the emission ZPL lines and (ii) the absorption ZPL lines are very sharp with a half-width of only 0.2 to 0.3 nm. This difference in linewidth between emission and absorption ZPL lines is due to the mixing of the excitation and emission beams in PL experiments, resulting in extrinsic broadening of the peaks. In Table III we compare the measured ZPL wavelengths with the calculated ones.

B. Defect assignment

The comparison of the ZPL PL spectra and the photo-EPR excitation spectra demonstrate that both agree in wavelength and thus allow us to assign the ZPL to each specific NV^- center (Fig. 7). The identification of the microscopic structure

TABLE III. Comparison of the ZPL lines in emission and absorption (experiment and DFT theory) and their assignment to the particular axial or basal NV center configuration deduced from the EPR spin Hamiltonian parameters.

ZPL label	ZPL absorption (nm), expt.	ZPL absorption linewidth (nm)	ZPL emission (nm), expt.	ZPL absorption (nm), DFT	Configuration (from EPR)
NV4 axial	1227.26	0.3	1227	1307	k_2k_1 axial
NV1 axial	–	–	1155	1244	k_1k_2 axial
NV2a axial	1182.62	0.2	1183	1284	hh axial
NV5 basal	1242.4	0.2	1242	1324	hk_1 basal
NV3 basal	1204.0	0.2	1204	1327	k_2k_2 basal
NV2b basal	1183.2	0.2	1183	1286	k_1h basal

of the NV centers was based on the EPR parameters. The point symmetry C_{3v} or C_{1h} allows us a direct distinction between axial and basal NV centers; the site assignment $(k1, k2, h)$ of each axial and basal NV^- center is based on theory predictions of their ZFS parameters and additionally confirmed by their calculated ZPL energies. Even though the absolute values of the calculated ZFS parameters are slightly lower than the experimental ones [cf. Table II and Fig. 8(a)], the trends are very well reproduced and we assign them according to these results. Note that by this assignment the trend in the vertical excitation energies is also well reproduced [see Fig. 8(b)]. A further element comforting the assignment is the consideration of the rhombic ZFS parameter E, which shows large differences in the three basal cases and is at least qualitatively reproduced in our calculations. In particular, we found that the center with medium D value ($k2k2$) shows the largest rhombicity E (cf. Table II).

V. CONCLUSION

The EPR-tagged high-resolution photoexcitation spectroscopy [40] based on the intracenter recombination induced ground state spin polarization has allowed us to associate the photoluminescence ZPL with the specific microscopic configurations of the axial and basal NV^- centers. The assignment of the paramagnetic NV^- centers is based on their spin Hamiltonian parameters, which have been obtained from *ab initio* calculations. Advanced calculations of the zero-field splitting parameter D, taking into account the spin contamination, have allowed us to further increase the accuracy with which the values can be obtained. As in the case of NV^- centers in 4*H*-SiC we observe a negligible Franck-Condon shift between the emission and absorption ZPL of the intracenter transition ${}^3E \rightarrow {}^3A_2$. With their long spin coherence times and their optical spectral range of 1.2 μm the NV centers in 6*H*-SiC should be promising candidates for QT applications.

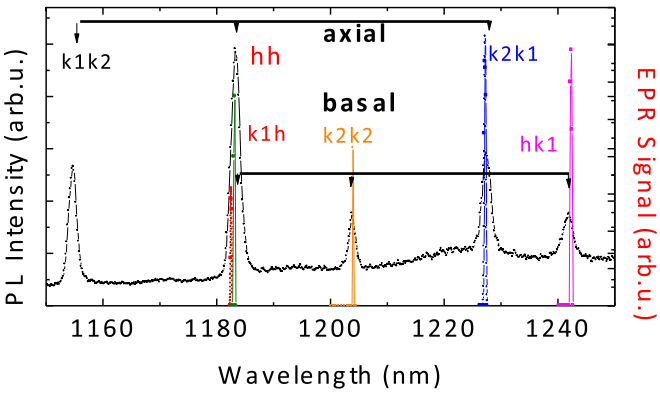

FIG. 7. Superposition of the photoluminescence ZPL (black line) and the absorption ZPL lines (color lines) as determined by high-resolution resonant excitation of the EPR spectra. The nearly degenerate ZPL of the axial (hh) and basal ($k1h$) NV^- centers are not resolved in the PL spectrum due to insufficient resolution.

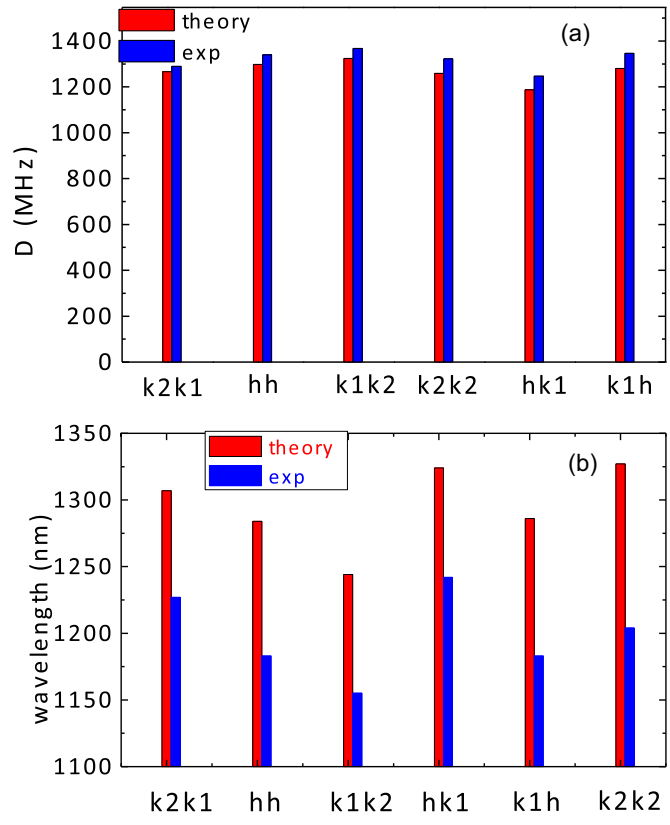

FIG. 8. (a), left: Comparison of experimental and calculated ZFS parameters D for the NV^- centers. (b), right: Comparison of the experimental and DFT-calculated absorption vertical ZPL wavelength of the six NV^- centers. As expected the PBE-calculated excitation energies are systematically underestimated by about 100 meV, but the trend is correctly reproduced.

ACKNOWLEDGMENTS

S.A.Z. wishes to acknowledge the support from the Merlion Grant France—Singapore and the Quantum Nanophotonic Laboratories at Nanyang Technical University. U.G. and T.B. acknowledge support from the Deutsche Forschungsgemeinschaft via priority program SPP 1601 (GE-1260/5-2).

[1] D. D. Awschalom, R. Hanson, J. Wrachtrup, and B. B. Zhou, Quantum technologies with optically interfaced solid-state spins, Nat. Photon. **12**, 516 (2018).

[2] J. R. Weber, W. F. Koehl, J. B. Varley, A. Janotti, B. B. Buckley, C. G. Van de Walle, and D. D. Awschalom, Quantum computing with defects, Proc. Natl. Acad. Sci. USA **107**, 8513 (2010).

[3] J. R. Weber, W. F. Koehl, J. B. Varley, A. Janotti, B. B. Buckley, C. G. Van de Walle, and D. D. Awschalom, Defects in SiC for quantum computing, J. Appl. Phys. **109**, 102417 (2011).

[4] A. Dzurak, Quantum computing: Diamond and silicon converge, Nature (London) **479**, 47 (2011).

[5] A. Boretti, Optical materials: Silicon carbide's quantum aspects, Nat. Photon. **8**, 88 (2014).

[6] L. Gordon, A. Janotti, and C. G. Van de Walle, Defects as qubits in 3*C*- and 4*H*-SiC, Phys. Rev. B **92**, 045208 (2015).

[7] S. E. Economou and P. Dev, Spin photon entanglement interfaces in silicon carbide defect centers, Nanotechnology **27**, 504001 (2016).

[8] S. Castelletto, L. Rosa, and B. C. Johnson, Silicon carbide for novel quantum technology devices, in *Advanced Silicon Carbide Devices and Processing* (2015), Chap. 8.

[9] W. F. Koehl, B. B. Buckle, F. J. Heremans, G. Calusine, and D. D. Awschalom, Room temperature coherent control of defect spin qubits in silicon carbide, Nature (London) **479**, 84 (2011).

[10] V. A. Soltamov, A. A. Soltamova, P. G. Baranov, and I. I. Proskuryakov., Room Temperature Coherent Spin Alignment of Silicon Vacancies in 4*H* and 6*H*-SiC, Phys. Rev. Lett. **108**, 226402 (2012).

[11] D. Riedel, F. Fuchs, H. Kraus, S. Väeth, A. Sperlich, V. Dyakonov, A. A. Soltamova, P. G. Baranov, V. A. Ilyin, and G. V. Astakhov, Resonant Addressing and Manipulation of Silicon Vacancy Qubits in Silicon Carbide, Phys. Rev. Lett. **109**, 226402 (2012).

[12] A. L. Falk, B. B. Buckley, G. Calusine, W. F. Koehl, V. V. Dobrovitski, A. Politi, C. A. Zorman, P. X.-L. Feng, and D. D. Awschalom, Polytype control of spin qubits in silicon carbide, Nat. Commun. **4**, 1819 (2013).

[13] M. Radulaski, T. M. Babinec, S. Buckley, A. Rundquist, J. Provine, K. Alasaad, G. Ferro, and J. Vuckovic, Photonic crystal cavities in cubic (3C) polytype silicon carbide films, Opt. Exp. **21**, 32623 (2013).

[14] L.-P. Yang, C. Burk, M. Widmann, S. Y. Lee, J. Wrachtrup, and N. Zhao, Electron spin decoherence in silicon carbide nuclear spin bath, Phys. Rev. B **90**, 241203 (2014).

[15] H. Kraus, V. A. Soltanov, F. Fuchs, D. Simin, A. Sperlich, P. G. Baranov, G. V. Astakhov, and V. Dyakonov, Magnetic field and temperature sensing with atomic-scale spin defects in silicon carbide, Sci. Rep. **4**, 5303 (2014).

[16] D. J. Christle, A. L. Falk, P. Andrich, P. V. Klimov, J.ul Hassan, N. T. Son, E. Janzen, T. Oshima, and D. D. Awschalom, Isolated electron spins in silicon carbide with millisecond coherence times, Nat. Mater. **14**, 160 (2015).

[17] A. L. Falk, P. V. Klimov, V. Ivady, K. Szasz, D. J. Christle, W. F. Koehl, A. Gali, and D. D. Awschalom, Optical Polarization of Nuclear Spins in Silicon Carbide, Phys. Rev. Lett. **114**, 247603 (2015).

[18] M. Widmann, S. Y. Lee, T. Rendler, N. T. Son, H. Fedder, S. Paik, L.-P. Yang, N. Zhao, S. Yang, I. Booker, A. Denisenko, M. Jamali, S. A. Momenzadeh, I. Gerhardt, T. Oshima, A. Gali, E. Janzen, and J. Wrachtrup, Coherent control of single spins in silicon carbide at room temperature, Nat. Mater. **14**, 164 (2015).

[19] P. V. Klimov, A. L. Falk, B. B. Buckley, and D. D. Awschalom, Electrically Driven Spin Resonance in Silicon Carbide Color Centers, Phys. Rev. Lett. **112**, 087601 (2014).

[20] O. V. Zwier, D. O'Shea, A. R. Onur, and C. H. van der Valle, All-optical coherent population trapping with defect spin ensembles in silicon carbide, Sci. Rep. **5**, 10931(2015).

[21] S. G. Carter, O. O. Soykal, P. Dev, S. E. Economu, and E. R. Glaser, Spin coherence and echo modulation of the silicon vacancy in 4*H*-SiC at room temperature, Phys. Rev. B **92**, 161202 (2015).

[22] P. V. Klimov, A. L. Falk, D. J. Christle, V. V. Dobrovitski, and D. D. Awschalom, Quantum entanglement at ambient conditions in a macroscopic solid-state spin ensemble, Sci. Adv. **1**, e1501015 (2015).

[23] H. Seo, A. L. Falk, P. V. Klimov, K. C. Miao, G. Galli, and D. D. Awschalom, Quantum decoherence dynamics of divacancy spins in silicon carbide, Nat. Commun. **7**, 12935 (2016).

[24] G. Calusine, A. Politi, and D. D. Awschalom, Cavity-Enhanced Measurements of Defect Spins in Silicon Carbide, Phys. Rev. Appl. **6**, 014019 (2016).

[25] D. Simin, H. Kraus, A. Sperlich, T. Ohshima, G. V. Astakhov, and V. Dyakonov, Long-lived quantum memory in silicon carbide with natural isotope abundance, arXiv:1602.05775v1

[26] A. Lohrmann, B. C. Johnson, J. C. McCallum, and S. Castelletto, A review on single photon sources in silicon carbide, Rep. Prog. Phys. **80**, 034502 (2017).

[27] D. Simin, H. Kraus, A. Sperlich, T. Oshima, G. V. Astakov, and V. Dyakonov, Locking of electron spin coherence above 20 ms in natural silicon carbide, Phys. Rev. B **95**, 161201 (2017).

[28] J. Wang, Y. Zhou, X. Zhang, F. Liu, K. Li, Z. Liu, G. Wang, and W. Gao, Efficient Generation of an Array of Single Silicon-Vacancy Defects in Silicon Carbide, Phys. Rev. Appl. **7**, 064021 (2017).

[29] D. J. Christle, P. V. Klimov, C. F. de la Casas, K. Szasz, V. Ivady, V. Jokubavicius, J. ul Hassan, M. Syväjärvi, W. F. Koehl, T. Oshima, N. T. Son, E. Janzen, A. Gali, and D. D. Awschalom, Isolated Spin Qubits in SiC with a High-Fidelity Infrared Spin-to-Photon Interface, Phys. Rev. X **7**, 021046 (2017).

[30] C. F. de las Casas, D. J. Christle, J. Ul Hassan, T. Oshima, N. T. Son, and D. Awschalom, Stark tuning and electrical charge state control of single divacancies in silicon carbide, Appl. Phys. Lett. **111**, 262403 (2017).

[31] Y. Zhou, J. Wang, X. Zhang, K. Li, and W. Gao, Self Protected Nanoscale Thermometry Based on Spin Defects in Silicon Carbide, Phys. Rev. Appl. **8**, 044015 (2017).

[32] R. Nagy, M. Widman, M. Niethammer, D. B. R. Dasari, I. Gerhardt, O. O. Soykal, M. Radulaski, T. Oshima, J. Vuckovic, N. T. Son, I. G. Ivanov, S. E. Economou, C. Bonato, S-Y. Lee, and J. Wrachtrup, Quantum Properties of Dichroic Silicon Vacancies in Silicon Carbide, Phys. Rev. Appl. **9**, 034022 (2018).

[33] J. Wang, Y. Zhou, Z. Wang, A. Rasmita, J. Yang, X. Li, H. J. von Bardeleben, and W. Gao, Bright room temperature single photon source at telecom range in cubic silicon carbide, Nat. Commun. **9**, 4106 (2018).

[34] S.-i. Sato, T. Narahara, Y. Abe, Y. Hijikata, T. Umeda, and T. Ohshima, Formation of nitrogen vacancy centers in 4*H*-SiC and their near infrared photoluminescence properties, J. Appl. Phys. **126**, 083105 (2019).

[35] M. W. Doherty, N. B. Masson, P. Delaney, F. Jelezko, J. Wrachtrup, and L. C. L. Hollenberg, The nitrogen vacancy colour center in diamond, Phys. Rep. **528**, 1 (2013).

[36] H. J. von Bardeleben, J. L. Cantin, E. Rauls, and U. Gerstmann, Identification and magneto-optical properties of the NV center in 4*H*-SiC, Phys. Rev. B **92**, 064104 (2015).

[37] H. J. von Bardeleben, J. L. Cantin, A. Csóré, A. Gali, E. Rauls, and U. Gerstmann, NV centers in 3*C*, 4*H*, and 6*H* silicon carbide: A novel platform for solid-state qubits and nanosensors, Phys. Rev. B **94**, 121202(R) (2016).

[38] H. J. von Bardeleben and J. L. Cantin, NV centers in silicon carbide: From theoretical predictions to experimental observation, MRS Commun. Res. Lett. **7**, 591 (2017).

[39] A. Csóré, H. J. von Bardeleben, J. L. Cantin, and A. Gali, Characterization and formation of NV centers in 3C, 4*H*, and 6*H*-SiC: An *ab initio* study, Phys. Rev. B **96**, 085204 (2017).

[40] S. A. Zargaleh, S. Hameau, B. Eble, F. Margaillan, H. J. von Bardeleben, J. L. Cantin, and W. Gao, Nitrogen vacancy center in cubic silicon carbide: A promising qubit in the 1.5 μm spectral range for photonic quantum networks, Phys. Rev. B **98**, 165203 (2018).

[41] S. A. Zargaleh, H. J. von Bardeleben, J. L. Cantin, U. Gerstmann, S. Hameau, B. Eble, and W. Gao, Electron paramagnetic resonance tagged high-resolution excitation spectroscopy of NV-centers in 4*H*-SiC, Phys. Rev. B **98**, 214113 (2018).

[42] J. F. Wang, F-F. Yan, Q. Li, Z. H. Liu, H. Liu, G.-P. Guo, L.-P. Guo, X. Zhou, J. M. Cui, J. Wang, Z. Q. Zhou, X.-Y. Xu, J.-S. Xu, C. F. Li, and G.-C. Guo, Coherent control of nitrogen vacancy center spins in silicon carbide at room temperature, arXiv:1909.12481.

[43] P. Giannozzi, S. Baroni, N. Bonini, M. Calandra *et al.*, QUANTUM ESPRESSO: A modular and open-source software project for quantum simulations of materials, J. Phys.: Condens. Matter **21**, 395502 (2009).

[44] P. Giannozzi, O. Andreussi, T. Brumme, O. Bunau *et al.*, Advanced capabilities for materials modeling with Quantum ESPRESSO, J. Phys.: Condens. Matter **29**, 465901 (2017).

[45] P. Perdew, K. Burke, and M. Ernzerhof, Generalized Gradient Approximation Made Simple. Phys. Rev. Lett. **77**, 3865 (1996).

[46] P. E. Blöchl, Projector augmented-wave method, Phys. Rev. B **50**, 17953 (1994).

[47] T. Biktagirov, W. G. Schmidt, and U. Gerstmann, Calculation of spin-spin zero-field splitting within periodic boundary conditions: Towards all-electron accuracy, Phys. Rev. B **97**, 115135 (2018).

[48] P. Jost and C. van Wüllen, Why spin contamination is a major problem in the calculation of spin-spin coupling in triplet biradicals, Phys. Chem. Chem. Phys. **15**, 16426 (2013).

[49] T. Biktagirov, W. G. Schmidt, and U. Gerstmann, Efficient scheme to eliminate spin contamination in magnetic dipolar coupling: Application to the zero-field splitting of NV^- centers, arXiv:1909.13577.

[50] Label translation due to interchanged $k1/k2$ for the C sublattice: The three axial NV centers labeled *hh*, $k1k1$, $k2k2$ in Refs. [38,41] have been substituted by *hh*, $k2k1$, $k1k2$; similarly for the basal ones $k2h$, $k1k2$, $hk1$ are replaced by $k1h$, $k2k2$, $hk1$, respectively.

[51] J. Davidsson, V. Ivady, R. Armiento, T. Oshima, N. T. Son, A. Gali, and I. A. Abrikosov, Identification of divacancy and silicon vacancy qubits in 6*H*-SiC, Appl. Phys. Lett. **114**, 112107 (2019).

[52] G. Thiering and A. Gali, *Ab initio* calculation of spin-orbit coupling for an NV center in diamond exhibiting dynamic Jahn-Teller effect, Phys. Rev. B **96**, 081115 (2017).

[53] A. Batalov, V. Jacques, F. Kaiser, P. Siyushev, P. Neumann, L. J. Rogers, R. L. McMurtrie, N. B. Manson, F. Jelezko, and J. Wrachtrup, Low Temperature Studies of the Excited State Structure of Negatively Charged Nitrogen-Vacancy Color Centers in Diamond, Phys. Rev. Lett. **102**, 195506 (2009).